Supporting information for

Regulation of solid-electrolyte interphases formation via Li_3PO_4 artificial layer for ultra-stable germanium anodes

Haifeng Yan, Kun Chao, Zhonghua Zhang*, Zhenfang Zhou, Yuanming Li, Xuguang Liu, Jing Liu, Xiaosong Guo, Changming Mao* and Guicun Li*

H.-F. Yan, C. Chao, Z.-H. Zhang, Z.-F Zhou, Y.-M. Li, X.-G Liu, J. Liu, X.-S. Guo, M.-C. Ming*, G.-C. Li*

College of Materials Science and Engineering, Qingdao University of Science and Technology, Qingdao 266042, Shandong, China

e-mail: guicunli@qust.edu.cn

M.-C. Ming*

e-mail: mcm@qust.edu.cn

	Etotal (Ha)	E_1 (Ha)	E_2 (Ha)	ΔE (eV)
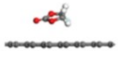 C, FEC	-2726.57140	-2285.17098	-441.38193	-0.50
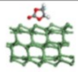 Ge, FEC	-149970.75857	-149529.35309	-441.38183	-0.64
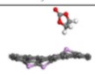 C/P, FEC	-3635.73283	-3194.32357	-441.38183	-0.75
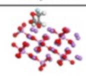 Li_3PO_4, FEC	-7091.79770	-6650.34230	-441.38055	-2.04

Figure S1 Calculated data on the binding energy of FEC molecules adsorbed on the surface of different materials, respectively.

	Etotal (Ha)	E_1 (Ha)	E_2 (Ha)	ΔE (eV)
 C, EC	-2627.34541	-2285.17098	-342.17429	-0.39
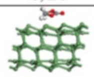 Ge, EC	-149871.54545	-149529.35309	-342.17429	-0.49
 C/P, EC	-3536.51372	-3194.32357	-342.17429	-0.43
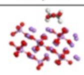 Li_3PO_4, EC	-6992.53023	-6650.34230	-342.17429	-0.37

Figure S2 Calculated data on the binding energy of EC molecules adsorbed on the surface of different materials, respectively.

The calculated adsorption energies of EC on the surfaces of C (001), Ge (111), P/C, and Li_3PO_4 (021) are -0.39 eV, -0.49 eV, -0.43 eV, and -0.37 eV, respectively.

	Etotal (Ha)	E_1 (Ha)	E_2 (Ha)	ΔE (eV)
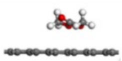 C, DMC	-2628.32624	-2285.17098	-343.13830	-0.46
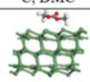 Ge, DMC	-149872.51020	-149529.35309	-343.13830	-0.51
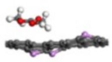 C/P, DMC	-3537.48252	-3194.32357	-343.13830	-0.56
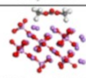 Li_3PO_4, DMC	-6993.49830	-6650.34230	-343.13830	-0.48

Figure S3 Calculated data on the binding energy of DMC molecules adsorbed on the surface of different materials, respectively.

The calculated binding energies of DMC on the surfaces of C (001), Ge (111), P/C, and Li_3PO_4 (021) are -0.46 eV, -0.51 eV, -0.56 eV, and -0.48 eV, respectively.

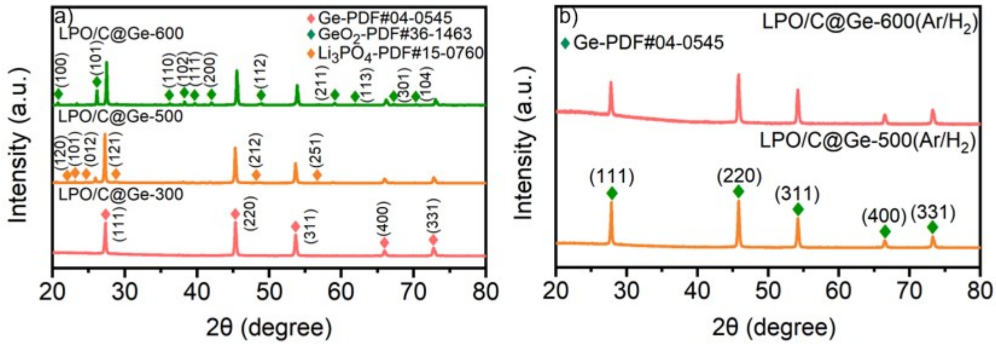

Figure S4 XRD patterns of the LPO/C@Ge in N_2 atmosphere (a) and Ar/H_2 atmosphere (b).

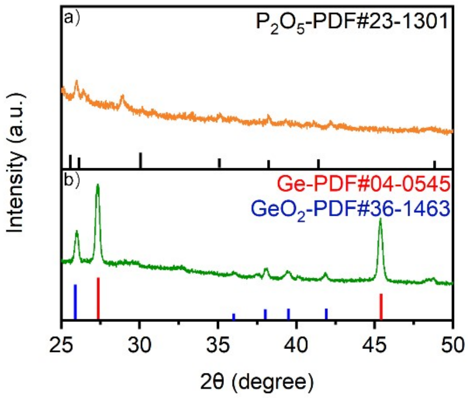

Figure S5 XRD patterns of the PA-400 (a) and 10P/C@Ge-400 (b).

The product of PA after annealing at 400°C is a composite of P_2O_5 and amorphous products. During the synthesis, a higher amount of PA was used in the P/C@Ge-400 sample (the ratio of PA to Ge was 1:4), and the results indicated the presence of trace amounts of P_2O_5 in the P/C@Ge-400 sample. These findings may suggest that PA is converted into phosphate oxides and a certain amount of P/C during the sample synthesis process.

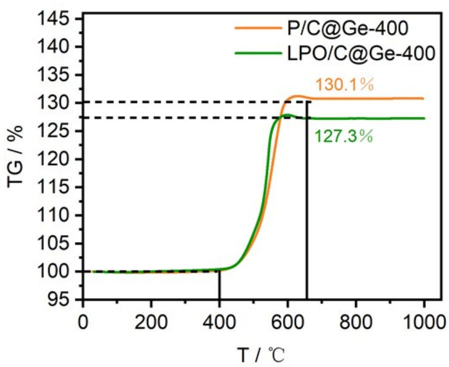

Figure S6 TG curve of LPO/C@Ge and P/C@Ge.

There is a weight increase during temperature increasing. In air condition, it is assumed that the P-doped carbon species in P/C@Ge sample are oxidized to be P_2O_5 (boiling point is around 360 °C) and CO_2, both of which are in gas states. Thus the oxidization of Ge to form GeO_2 contributes to the main weight increase during 400~650 °C. According to this assumption, the carbon content is calculated to be 9.7%. As for LPO/C@Ge sample, it is hard to determine the actual content of carbon species because of the influence of Li_3PO_4. Thus, the carbon content is determined to be <11.6% based on above assumption.

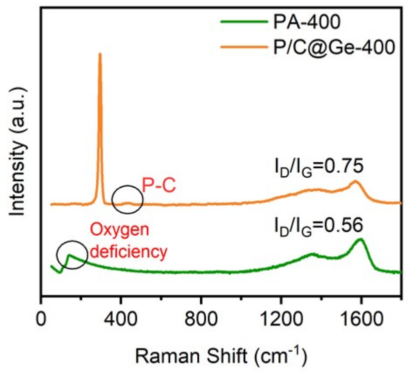

Figure S7 Raman spectra of PA-400 and P/C@Ge.

The peak at 150 cm^{-1} in PA-400 corresponds to a large number of oxygen vacancies, which is attributed to P_2O_5. No distinct signal for P-doped carbon (350-450 cm^{-1}) is observed. In contrast, the peak at 420 cm^{-1} in P/C@Ge-400 is assigned to P-doped carbon. The analysis of the D and G bands indicates that PA-400 has a higher degree of graphitization, while the higher defect density in P/C@Ge-400 is attributed to P doping, indirectly corroborating the aforementioned conclusion.

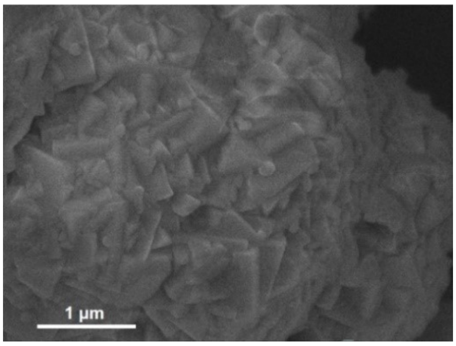

Figure S8 SEM image of GeO_2 pristine.

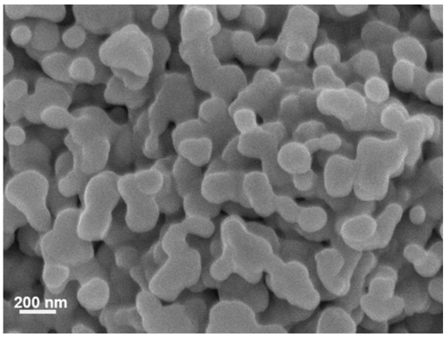

Figure S9 SEM image of bare Ge particle.

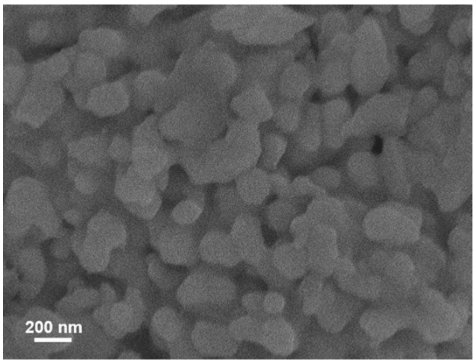

Figure S10 SEM image of LPO/C@Ge particle.

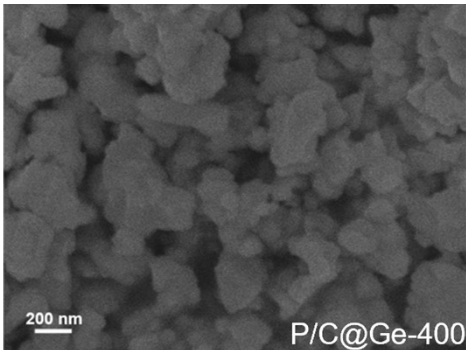

Figure S11 The SEM images of P/C@Ge-400.

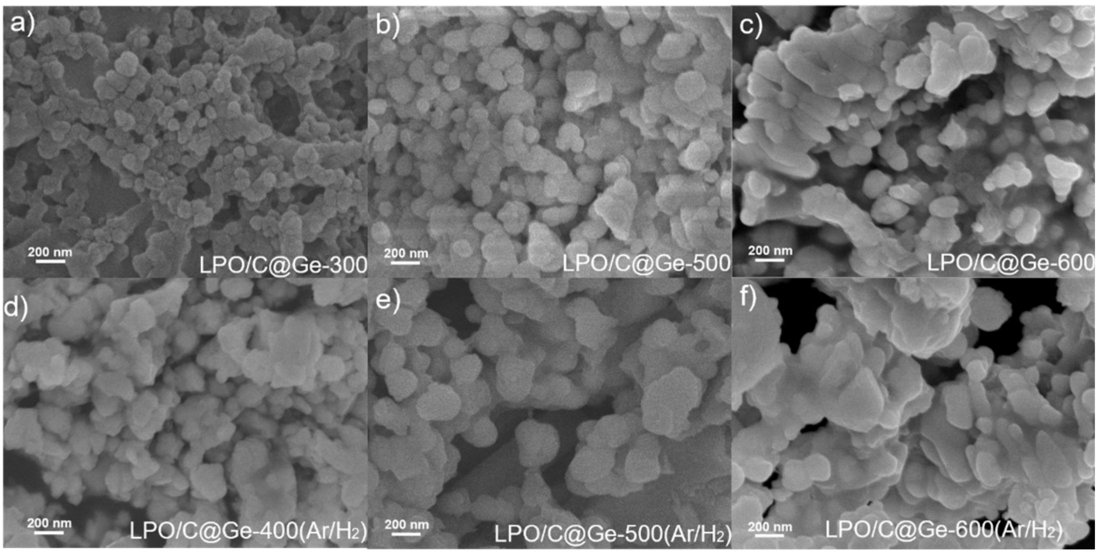

Figure S12 The SEM images of LPO/C@Ge thermally annealed at different temperatures and atmospheres. (a) 300 ℃ (N_2), (b) 500 ℃ (N_2), (c) 600 ℃ (N_2), (d) 400℃ (Ar/H_2), (e) 500 ℃ (Ar/H_2), (f) 600 ℃ (Ar/H_2).

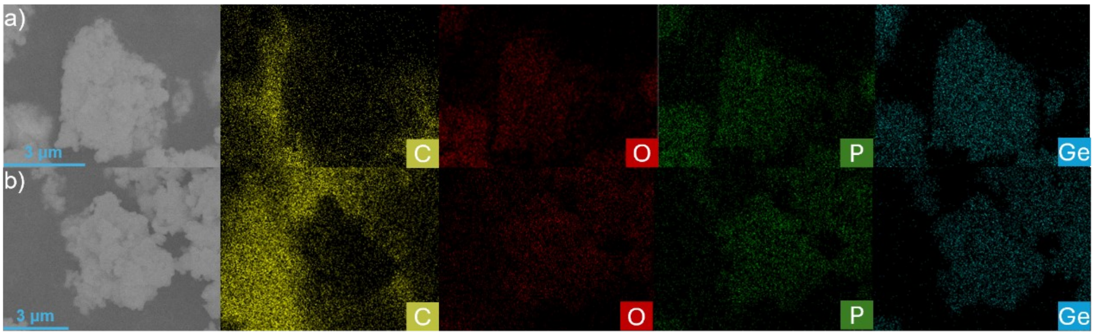

Figure S13 EDS-mapping images of LPO/C@Ge (a) and P/C@Ge (b).

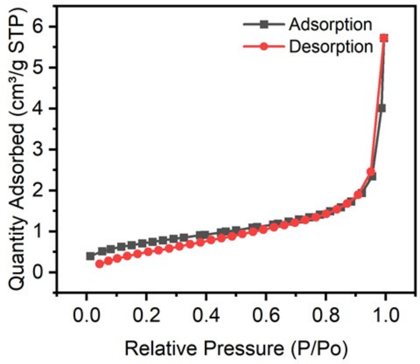

Figure S14 The N_2 adsorption and desorption curves of P/C@Ge.

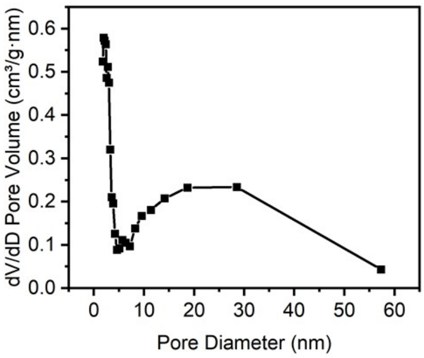

Figure S15 The corresponding pore-size distribution of P/C@Ge.

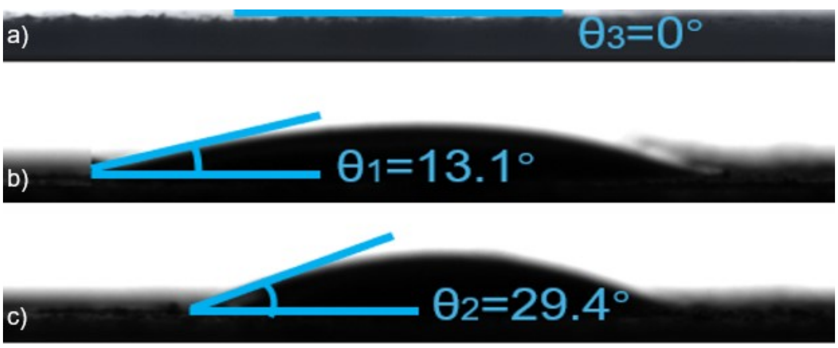

Figure S16 The contact angles measurements of bare Ge (a), LPO/C@Ge (b) and P/C@Ge (c).

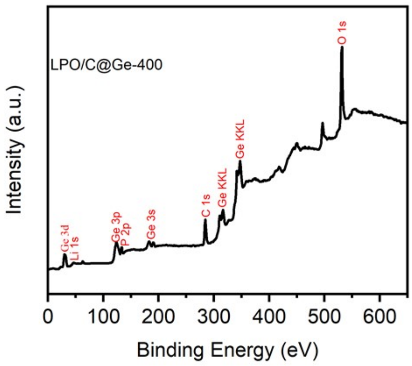

Figure S17 Survey scan XPS spectra of LPO/C@Ge.

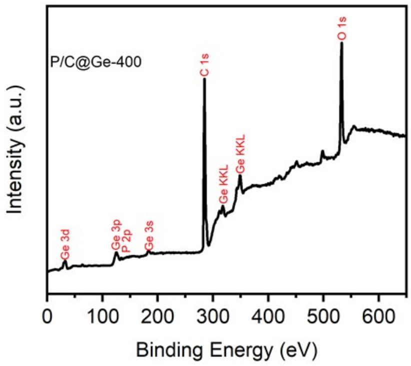

Figure S18 Survey scan XPS spectra of P/C@Ge.

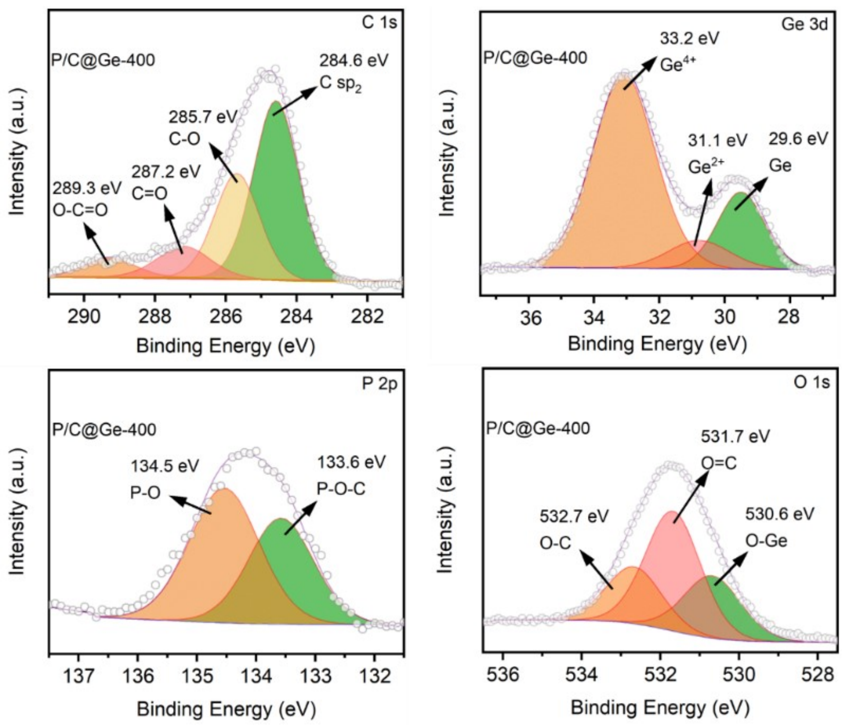

Figure S19 High resolution XPS spectrum of P/C@Ge.

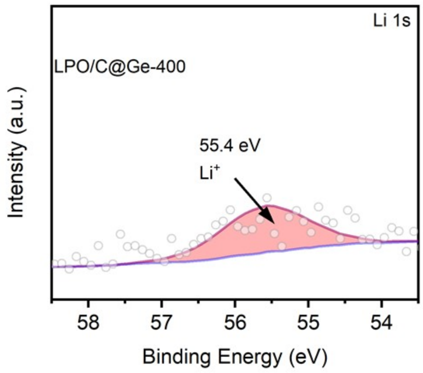

Figure S20 High resolution Li 1s XPS spectrum of LPO/C@Ge.

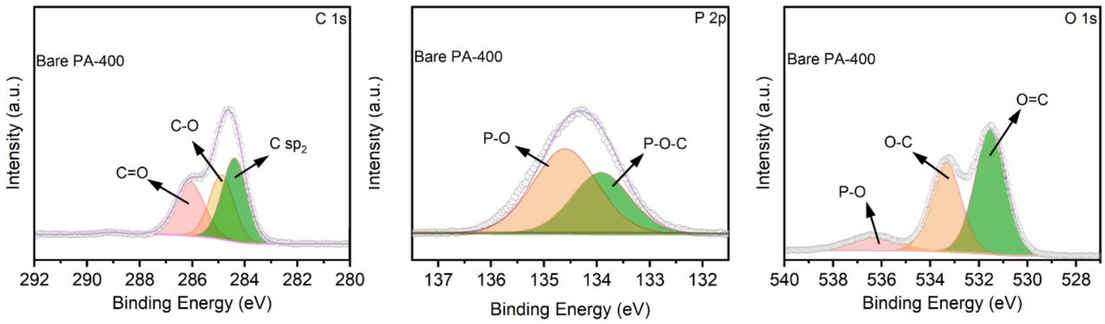

Figure S21 High resolution XPS spectrum of PA-400.

During the sintering process, the O_2 generated from the decomposition of PA reacts with Ge to form Ge-O bonds, preventing P from coordinating and leading to the formation of P-doped carbon. In the bare PA sample, this results in the formation of P_2O_5. Compared with P/C@Ge-400, PA-400 exhibits weaker binding between C and O, and stronger binding between P and O, indicating that P_2O_5 is the dominant form of phosphorus in PA-400, while P-C is the main form of phosphorus in P/C@Ge-400.

Table S1 Previously reported cycle performance of the Ge anode.

Samples	Current density	Initial capacity	Initial coulombic efficiency	Capacity (after cycling)	Ref.
Ge nanowires	0.3 A g^{-1}	1284.3 mAh g^{-1}	79.6%	1058.9 mAh g^{-1} (300^{th})	5
Sp-Ge/C-Pitch	1.0 A g^{-1}	1013.0 mAh g^{-1}	82.7%	645.0 mAh g^{-1} (300^{th})	10
Ge@B-PAALi	1.0 A g^{-1}	1254.9 mAh g^{-1}	75.1%	1053.8 mAh g^{-1} (500^{th})	12
Ge/Co_3O_4 nanorod	1.0 A g^{-1}	1445.0 mAh g^{-1}	24.6%	1171.0 mAh g^{-1} (298^{th})	15
Ge/rGO/CNTs	0.5 A g^{-1}	983.4 mAh g^{-1}	60.5%	614.5 mAh g^{-1} (300^{th})	16
Ge@N-CNTs	0.1 A g^{-1}	1176.0 mAh g^{-1}	68.0%	892.0 mAh g^{-1} (200^{th})	21
Ge/CNFs	1.0 A g^{-1}	1297.0 mAh g^{-1}	49.6%	1050.0 mAh g^{-1} (100^{th})	22
LPO/C@Ge	1.0 A g^{-1}	1255.5 mAh g^{-1}	80.1%	1202.2 mAh g^{-1} (600^{th})	This work

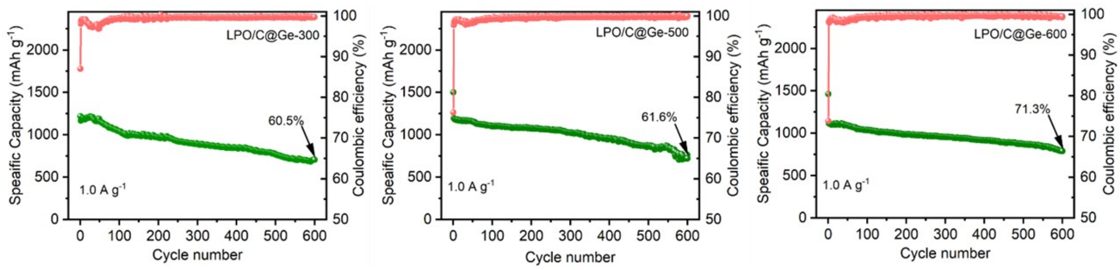

Figure S22 Cycling performance of LPO/C@Ge at a current density of 1.0 A g^{-1} under different temperatures (N_2 atmospheres).

Combined with the XRD results, the difference in properties suggests that the temperature and atmosphere during annealing are key factors in the formation of Li_3PO_4 and GeO_2.

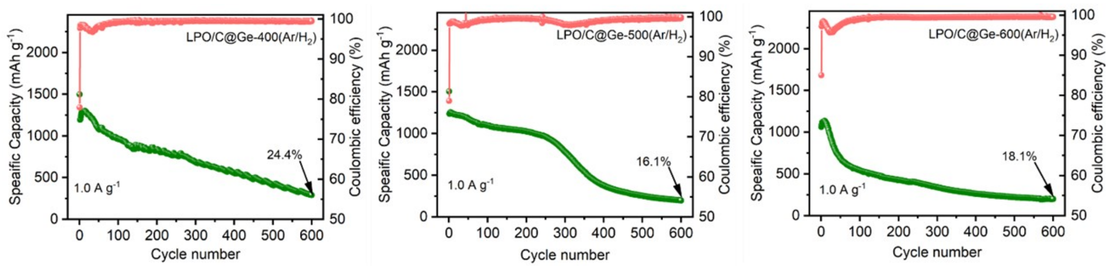

Figure S23 Cycling performance of LPO/C@Ge at a current density of 1.0 A g^{-1} under different temperatures (Ar/H_2 atmospheres).

Although the use of a reductive atmosphere during annealing can prevent the formation of

GeO_2, it impedes the cycling performance.

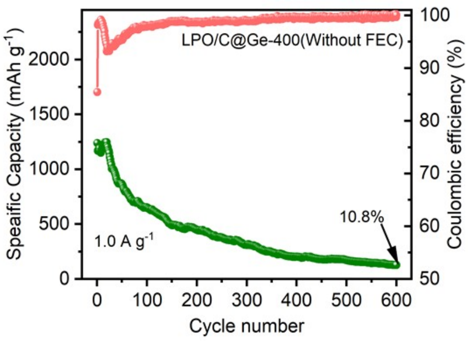

Figure S24 Cycling performance of LPO/C@Ge at a current density of 1.0 A g^{-1} under N_2 atmospheres (without FEC).

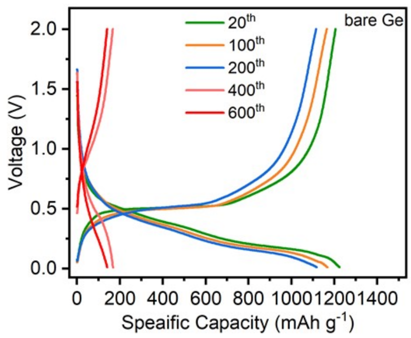

Figure S25 The cyclic voltammetric curves of bare Ge at the 20th, 100th, 200th, 400th and 600th cycles at a current density of 1.0 A g^{-1}.

Table S2 Previously reported rate performances of Ge anode.

Samples	Initial current density	Initial capacity	High current density	Capacity retention	Ref.
Ge nanowires	0.3 A g^{-1}	1033.5 mAh g^{-1}	3.0 A g^{-1}	59.5%	5
Sp-Ge/C-Pitch	0.2 A g^{-1}	1062.3 mAh g^{-1}	5.0 A g^{-1}	65.8%	10
Ge@B-PAALi	0.5 A g^{-1}	1214.6 mAh g^{-1}	5.0 A g^{-1}	79.3%	12

Ge/Co_3O_4 nanorod	0.5 A g^{-1}	1237.0 mAh g^{-1}	5.0 A g^{-1}	63.6%	15
Ge/rGO/CNTs	0.1 A g^{-1}	1051.5 mAh g^{-1}	2.0 A g^{-1}	52.3%	16
Ge@N-CNTs	0.1 A g^{-1}	1145.0 mAh g^{-1}	3.2 A g^{-1}	74.2%	21
Ge/CNFs	0.2 A g^{-1}	1330.0 mAh g^{-1}	5.0 A g^{-1}	55.4%	22
LPO/C@Ge	0.5 A g^{-1}	1327.4 mAh g^{-1}	5.0 A g^{-1}	93.1%	This work

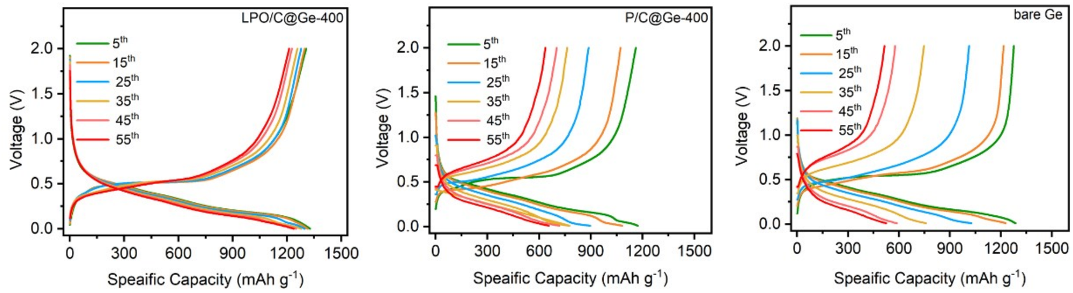

Figure S26 The Cyclic voltammetry curves of LPO/C@Ge, P/C@Ge and bare Ge at different rates (0.5, 1, 2, 3, 4 and 5 A g^{-1}).

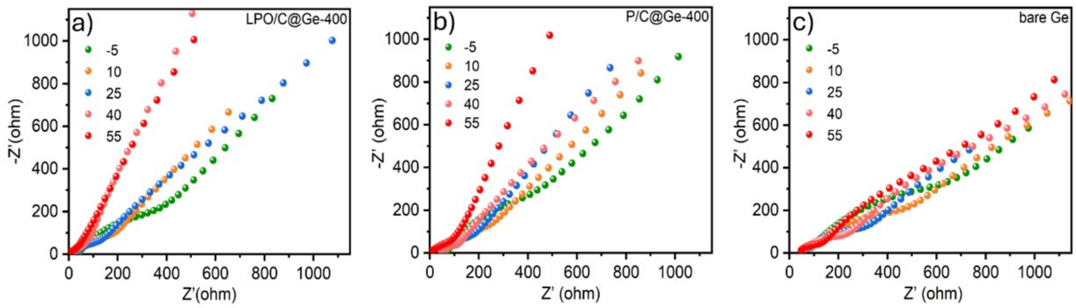

Figure S27 EIS of LPO/C@Ge (a), P/C@Ge (b), and bare Ge (c) at different temperatures.

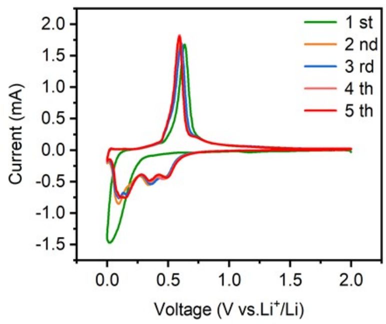

Figure S28 The CV curves of P/C@Ge at scan rate of 0.1 mV s^{-1}.

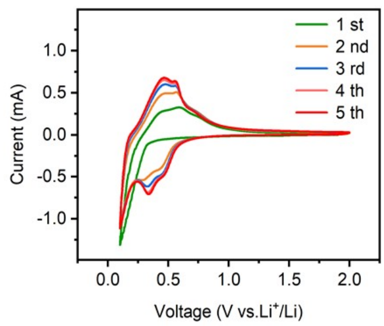

Figure S29 The CV curves of bare Ge at scan rate of 0.1 mV s $^{-1}$.

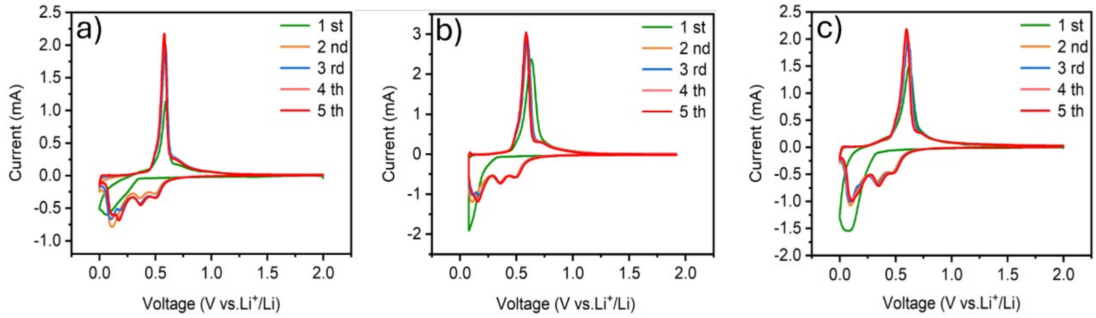

Figure S30 The CV curves of LPO/C@Ge-300 (a), LPO/C@Ge-500 (b) and LPO/C@Ge-600 (c) at scan rate of 0.1 mV s $^{-1}$.

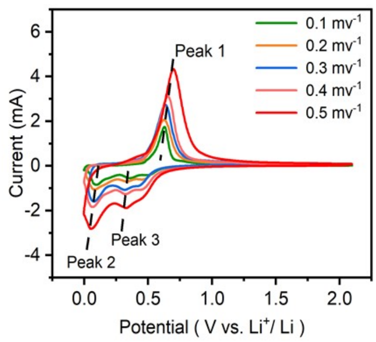

Figure S31 The CV curves of the P/C@Ge at different scan rates.

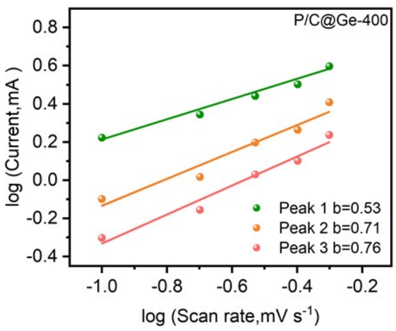

Figure S32 The plots of log (I) vs. log (v) (I: peak current; v: scan rate. The values of I and v are derived from Figure S23).

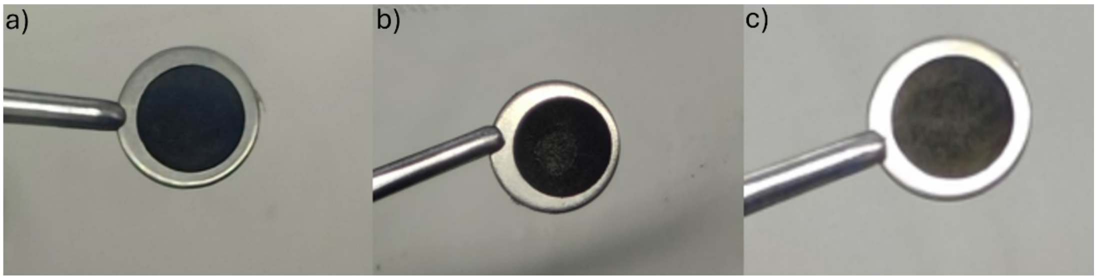

Figure S33 Photographs of LPO/C@Ge, P/C@Ge and bare Ge cathodes after 100 cycles.

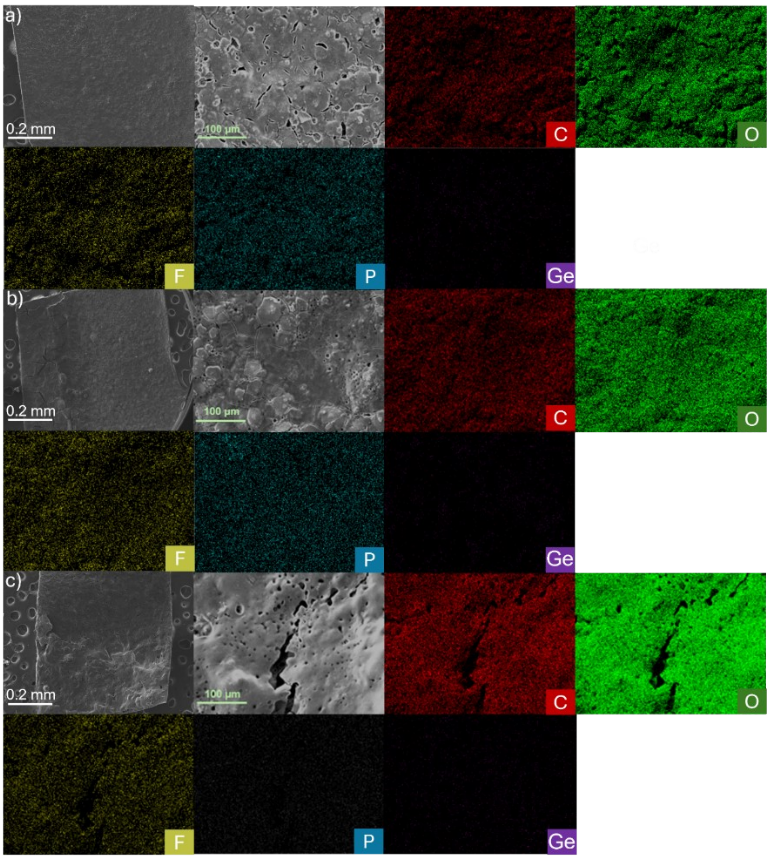

Figure S34 In-situ scanned images and EDS of the LPO/C@Ge, P/C@Ge and bare Ge cathodes after 100 cycles.